Nat. Hazards Earth Syst. Sci. Discuss., 3, 161–201, 2015
www.nat-hazards-earth-syst-sci-discuss.net/3/161/2015/
doi:10.5194/nhessd-3-161-2015

Natural Hazards and Earth System Sciences
Open Access
Discussions

Structure, stability and tsunami hazard associated with a rock slope in Knight Inlet, British Columbia

D. P. van Zeyl[1], D. Stead[1], M. Sturzenegger[1], B. D. Bornhold[2], and J. J. Clague[1]

[1]Department of Earth Sciences, Simon Fraser University, Burnaby, British Columbia, Canada
[2]Brian D. Bornhold Inc., Ladysmith, British Columbia, Canada

Received: 28 November 2014 – Accepted: 12 December 2014 – Published: 7 January 2015

Correspondence to: D. P. van Zeyl (vanzeyl@jdmollard.com)

Published by Copernicus Publications on behalf of the European Geosciences Union.

Abstract

Rockfalls and rockslides during the past 12 000 years have deposited bouldery debris cones on the seafloor beneath massive rock slopes throughout the inner part of Knight Inlet. The 885 m high rock slope situated across from the Kwalate site, a former First Nations village destroyed in the late 1500s by a slide-induced wave, exposes the contact between a Late Cretaceous dioritic pluton and metamorphic rocks of the Upper Triassic Karmutsen Formation. The pluton margin is strongly foliated in parallel with primary and secondary fabrics in the metamorphic rocks, resulting in highly persistent brittle structures. Other important structures include a set of sheeting joints and highly persistent mafic dykes and faults. Stability analysis identified the potential for planar and wedge failure. We made empirical estimates of impulse waves generated by potential slides ranging in size from 0.5 to 3.5 Mm^3, with results suggesting mid-inlet wave heights in the order of 6 to 26 m. As several similar rock slopes fronted by large submarine debris cones exist in the inner part of Knight Inlet, it is clear that tsunami hazards should be considered in coastal infrastructure development and land-use planning in this area.

1 Introduction

The inlets on the British Columbia (BC) coast are likely to see future development in the form of fish farms, power generation, transmission lines, pipelines, roads, and other coastal infrastructure, yet the hazards to this development remain underappreciated because the region, until recently, has been remote and sparsely populated. Historical observations in similar mountainous coastal and lacustrine environments have shown that tsunamis generated by subaerial landslides are common and can be highly destructive. For instance, Huber (1982) reported over 500 fatalities associated with about 50 subaerial landslides that generated displacement waves in lakes and reservoirs in Switzerland over the past 600 years. Slide-induced waves have claimed more than 200

NHESSD
3, 161–201, 2015

lives in the past 320 years in Norway (Blikra et al., 2005) and 10 lives in April 2007 in southern Chile (Sepúlveda et al., 2010). Damaging waves induced by subaerial landslides have also occurred on the coasts of Alaska (Miller, 1960a, b) and Greenland (Dahl-Jensen et al., 2004).

Extending to within 40 km of the highest ice-covered peaks in the Coast Mountains (Fig. 1), Knight Inlet is one of the longest and deepest fjords on the BC coast. Its precipitous, high walls are susceptible to rockfalls and rockslides, and several landslide deposits have been identified (van Zeyl, 2009) on the seafloor beneath these slopes (Fig. 2), suggesting that the inlet has been prone to landslide-generated tsunamis over the past 12 000 years. A recent study integrating archaeological and geological observations with oceanographic analysis suggests that the former village of Kwalate, located on the shoreline of Knight Inlet, was destroyed by a slide-induced wave in the late 1500s, with the possible loss of as many as 100 lives (Bornhold et al., 2007).

Expanding on the work of van Zeyl (2009), this paper documents the geology and stability of the rock slope across the inlet from the Kwalate village (Fig. 2), which is the likely source for the late 1500s tsunami. We also provide estimates of the height of waves generated by potential future slope failures at this site. The study provides a glimpse into the geological and morphological conditions encountered in an area of the BC coast suspected to be particularly prone to tsunamis generated by subaerial landslides.

2 Regional setting

The Coast Mountains form a belt of crystalline and metamorphic rocks 1600 km long and up to 150 km wide, bordering the Pacific Ocean from Alaska to the Fraser Lowland near Vancouver. They rise abruptly from the sea, and towards the axis of the range are characterized by rugged peaks and saw-toothed ridges. Numerous fjords, some more than 600 m deep, dissect the western margin of the Coast Mountains (Fig. 1).

NHESSD
3, 161–201, 2015

The steep-walled fjords of the BC coast are former Tertiary river valleys that were greatly deepened and widened by glaciers during the Pleistocene (Clague, 1991; Mathews, 1991). The last (Late Wisconsinan) glaciers of the Cordilleran ice sheet retreated eastward from the coast about 13 000 to 14 000 years ago, and Knight Inlet was probably ice-free by about 11 000 years ago (Clague, 1981; Dyke, 2004).

With a length of 125 km, Knight Inlet is one of the longest inlets on the BC coast (Fig. 1). It has a maximum depth of about 525 m and typical widths in the range of 2–4 km. The outer part of the inlet extends 70 km westward, whereupon it bends to the north and winds its way through terrain of considerably higher relief within the inner part of the inlet.

Van Zeyl (2009) identified postglacial submarine rockfall and rockslide deposits on the seafloor within the inner part of Knight Inlet (Fig. 2). The blocky conical deposits are present beneath steep mountainsides extending as high as 1200 m a.s.l. within one lateral kilometre of the shoreline. The deposits must have formed after deglaciation, and thus during the past 12 000 years, but nothing more is known about their age or history. One possibility is that rockfall and rockslide activity that produced many of these deposits was higher during the early Holocene as an immediate response to glacial debuttressing (cf. Evans and Clague, 1994). Another possibility is that activity increased in the second half of the Holocene after thousands of years of progressive rock-slope deformation and fatigue (Bjerrum and Jørstad, 1968) before the fjord walls could collapse. Knight Inlet lies within one of the most seismically active regions in Canada (Adams and Atkinson, 2003) – earthquakes are concentrated along or near the North American plate boundary, associated with the Cascadia subduction zone (Fig. 1), 200 km west of Knight Inlet, and the Queen Charlotte transform fault, 400 km to the northwest.

The maritime temperate climate of the southern mainland BC coast is characterized by average annual temperatures and monthly precipitation totals at sea level of about 8–10 °C and 1100–1800 mm, respectively (Environment Canada, 2008). The wet season (October–February), with monthly precipitation totals in excess of 500 mm and

NHESSD
3, 161–201, 2015

monthly mean temperatures as low as 0 to −5 °C, could render the area more susceptible to rockfalls and rockslides.

3 Methodology

3.1 Structural observations

We conducted fieldwork at the rock slope at Adeane Point during two site visits. We mapped major structures exposed along the crest of the slope, performed four scanlines in the central gully, and made additional structural observations at outcrops in the central and west gullies and at the base of the east wall (Figs. 3 and 4). The scanlines involved measuring and describing each discontinuity at least 25 cm in length that intersected a tape measure extending across an outcrop. We also made structural observations during traverses on the west slope, extending from the west gully to the crest of the rock slope. Georeferenced air photographs, digital elevation models, stereoscopic aerial photographs from the 1950s through the 1990s, and scaled oblique photographs provided additional structural information.

3.2 Rock mass conditions

We assessed rock mass conditions using Rock Quality Designation (RQD; Deere et al., 1967) and the Geological Strength Index (GSI; Marinos et al., 2005). RQD represents the percentage of intact core pieces larger than 10 cm to the length of core run or scanline. The GSI is used to derive field-scale rock mass properties for use in continuum rock mechanics modelling (Hoek et al., 2002). Intact rock uniaxial compressive strength was estimated in the field using a rock hammer (ISRM, 1978).

NHESSD
3, 161–201, 2015

3.3 Geomorphic analysis

Data on the morphology of the fjord were derived from digital elevation models. We used Canadian Digital Elevation Data (CDED) 20 m resolution elevation models (GeoBase, 2008) to analyze the terrestrial parts of the fjord. A 2 m resolution elevation model generated from multibeam echo-sounding data provided by the Canadian Hydrographic Service (2008) allowed us to analyze the submarine parts of Knight Inlet.

3.4 Stability analysis

A kinematic analysis was performed to identify possible modes of rock slope failure. We used geologic structure and slope morphology displayed in stereographic projections to evaluate the potential for planar, wedge, and toppling failure (Hoek and Bray, 1981; Wyllie and Mah, 2003). We then analyzed selected planar and wedge failure modes identified from kinematic analysis using the program SWEDGE (Rocscience, 2008) to compute the factor of safety of rigid blocks bounded by intersecting discontinuities. This analysis allowed us to rank the key failure types in terms of relative stability and to help estimate possible landslide volumes. The procedure involved computing the factor of safety for each failure type over the full range of slopes and aspects observed at the site. The analysis assumed no tension crack, an upper slope of 15° with the same aspect as the lower slope, a friction angle of 30°, and no cohesion. Although pore pressure fluctuations and earthquake accelerations are undoubtedly associated with progressive failure and likely are common triggering mechanisms for rock slope failures in this environment, these factors were not considered in this preliminary stability analysis.

NHESSD
3, 161–201, 2015

4 Rock slope characterization

4.1 Slope morphology

The north part of the unnamed mountain at Adeane Point is a bowl-shaped erosional basin that has a distinct U-shape in plan with a radius of curvature at the crest of the rock slope of about 400 m (Figs. 4 and 5). The surface area of the terrestrial portion of this erosional basin is about 1.5 km^2, a third of which is exposed bedrock.

A north-south line extending through the centre of the rock slope can be used to divide the basin into four main geometric components (Figs. 3–5): a NNE-dipping forested slope ("west slope"); a north-dipping rock wall ("west wall"); a WNW dipping rock wall ("east wall"); and a WNW-dipping forested slope ("east slope"). The west slope and its submarine extension are controlled by primary and secondary fabrics in the underlying metamorphic rocks, whereas the orientation of the east wall is controlled by a set of sheeting joints in the underlying diorite, and the west wall is controlled mainly by a complex of sub-vertical structures, which include mafic dykes and faults.

The maximum elevation at Adeane Point is 885 m at the east peak. Based on the DEM, relief from seafloor to summit is about 1400 m, with an average slope of about 45° (Fig. 6); the angle from the shoreline to the top of the slope is 55°, and local slope angles are as great as 70–72° near the tops of the east and west walls (Fig. 5).

4.2 Slope deposits

The submarine debris cone at the base of the slope dips 20–24°; it has a surface area of about 0.1 km^2 (Fig. 4) and an estimated volume of 3.5 Mm^3. Our analysis of images collected by Bornhold et al. (2007) from a remotely operated vehicle indicates that the debris cone comprises openwork, subangular blocks less than 2 m across that are dominantly 0.1–0.4 m in size.

We examined slope deposits in the central and west gullies (Fig. 2). The west gully lies largely within metamorphic rocks and its source area is the west wall. Grass,

NHESSD
3, 161–201, 2015

lichens, and seedlings are present on the deposit, suggesting minimal recent rockfall activity from its source area. In contrast, vegetation is generally absent in the central gully below the east wall; no lichens and mosses were observed on blocks, and the blocks are less weathered than those in the west gully, suggesting greater rockfall activity from the east wall. Oblique photographs also indicate a larger number of fresh rockfall scars on the east wall than on the west wall.

4.3 Bedrock geology

Rocks at Adeane Point consist of greenstone of the Upper Triassic Karmutsen Formation and Late Cretaceous diorite (Roddick and Woodsworth, 2006). The greenstone is massive to foliated and contains intercalations of marble, sandstone, argillite, phyllite, biotite-chlorite schist, and amphibolite (Bancroft, 1913; Roddick, 1977). The dioritic pluton exposed in the rock slope contains screens of amphibolites and schist, and is in sharp contact with the greenstone (structure 1a, Fig. 7), and both the diorite and greenstone are foliated near the contact.

4.4 Structural geology

4.4.1 Major structures

Portions of some of the major structures exposed in the rock slope (Figs. 7 and 8) were accessed from the top of the slope, and additional information on major structures was obtained from oblique photographs taken from a helicopter and from ground locations.

The most apparent and persistent structures, which we term set 1, are parallel to the foliation. At the crest of the slope, the four largest and most evident of these structures, labelled 1a, 1b, 1c, and 1d, are spaced about 50 m apart and are at least 100 m long (Figs. 7 and 8). Field measurements of three of them indicate an average attitude of 54/028° (dip/dip direction). Structure 1a extends the full height of the rock slope, with

NHESSD
3, 161–201, 2015

locally recessed portions of this structure suggesting the presence of weak layers or a fault zone.

A singular structure, labelled 2a, is exposed in a rockfall scar near the slope crest. It has roughly the same orientation as a distinct set of sheeting joints (set 2) and extends out of the scar and persists for at least 100 m, forming a potential sliding plane beneath a large rock mass encompassing the west peak (Figs. 7 and 8). The lower part of this structure, beneath the west peak, is noticeably curvi-planar and does not appear to intersect structure 1a.

4.4.2 Foliation

Foliation joints (set 1) in the intrusive and metamorphic rocks are some of the most persistent structures exposed in the rock slope. The average orientation of the foliation is 55/027° (Fig. 9f).

The attitudes of the subaerial portion and submarine extension of the west slope, as measured from the digital elevation models (Figs. 5 and 9b), are similar to outcrop foliation measurements (Fig. 9f). For instance, the SONAR data show that the average orientation of a large portion of the submarine extension of the west slope is 47/023°.

The foliation at Adeane Point is typical of foliation elsewhere in the southern Coast Belt, where structures in plutons and pendants are dominated by northwest-trending foliation that commonly dips steeply northeast (Woodsworth et al., 1991). Most plutonic rocks exhibit some degree of foliation, best developed near pluton margins (Roddick and Hutchison, 1974).

4.4.3 Bedding

Bedding in marble in the west gully and on the west slope generally dips steeply to the north and east (Fig. 9g). The variability in dip is due to ductile deformation of marble around black argillite lenses in the west gully. The average bedding attitude of 48/044° is similar to that of the foliation discussed above and to measurements made in marble

NHESSD
3, 161–201, 2015

and argillite at the site by Bancroft (1913). The coplanar nature of bedding and foliation is further accentuated by foliation-parallel layers of schist and massive greenstone up to several metres thick observed in the central gully.

Given that bedding is parallel to foliation and that weak rocks such as argillite and phyllite have been observed in the metamorphic belt exposed at this site (Roddick, 1977), weak layers parallel to the foliation are probably present within the rock slope, and faulting may have occurred along these layers during emplacement of the pluton. Indeed, we observed fault-like structures beneath extensive foliation-parallel beds of massive greenstone in the central gully, and many more may exist than were observed in the field. It is almost impossible to determine whether faults exist in areas where the stratified rocks occur in thin beds (Bancroft, 1913).

4.4.4 Sheeting joints

A single structure (2b) associated with a distinct set of sheeting joints (set 2) exposed near the crest has an attitude of 55/273°. In contrast, we observed gentler dips for this set in scanlines (Fig. 9d) and spot surveys at lower elevations, suggesting that the attitude of these joints conforms to the overall shape of the slope. Oblique photographs of the large rockfall scar at the crest show that the most visually apparent structures of set 2 are typically about 12 m long with a spacing of about 3 m. The digital elevation model illustrates how the orientation of the east wall is similar to the orientation of this joint set (Fig. 9c).

Terzaghi (1962) referred to sheeting joints as "valley joints", because they generally conform to the shape of the valley in which they occur. Bjerrum and Jørstad (1968) identified them as an important control on rockslides and rockfalls in the fjords of Norway, and they are one of the main causes of rockfalls and rockslides along BC Highway 99 between Vancouver and Whistler (Hoek and Bray, 1981; Gilbert, 2008).

NHESSD
3, 161–201, 2015

4.4.5 Mafic dykes

Mafic dykes cut both metamorphic and intrusive rocks. They range in thickness from about 15 cm to 2 m and consist of very strong to extremely strong, greenish-grey basalt. The dykes and the structures along which they were emplaced display great persistence; some of them were traced through the entire height of the west wall. The high degree of fracturing in the dykes compared to the adjacent host rock likely renders them as hydraulic conduits, which is supported by the presence of springs emanating from dykes at the apex of the central gully. Some of the dykes are parallel to the foliation (44/036°), whereas others cut across it (84/311°) (Fig. 9h).

Northwest- and northeast-trending dykes and brittle faults of Tertiary age are common along this part of the coast (Woodsworth et al., 1991). According to Bancroft (1913, p. 116), the dykes in this area "are frequently irregular in their strike, but the greater number of them either assume a direction which is parallel or transverse to the trend of the Coast Range", and "where the walls of the fiord are devoid of vegetation, these dykes often appear as dark, ribbon-like bands of a remarkably constant width, extending from the shoreline to the summit of mountains several thousand feet high."

4.4.6 Discontinuity system

To facilitate stability analysis, we developed a simple representation of the main discontinuity sets at this site based on the structures described above and on some additional structural details provided below (Table 1, Fig. 9i).

Foliation, bedding, and associated faults form S1, and sheeting joints form S2. Scanlines and spot measurements provide evidence of a north-trending sub-vertical set (S3) of joints and quartz veins, as well as a set of joints and quartz veins (S4) dipping about 45° SSE (Fig. 9d, e). A pronounced set of north-trending lineaments observed a few kilometres south of the site may be related to the sub-vertical joints defined here as S3.

NHESSD
3, 161–201, 2015

Because the strike of the dykes and similarly oriented structures and linear topographic features at Adeane Point differ substantially, we defined two sub-vertical discontinuity sets to incorporate this variability into the stability analysis (S5 and S6). We defined S5 based on ENE-trending, sub-vertical joints and dykes intersected in scanlines, ENE-trending linear cliffs 100–150 m high on the submarine sidewall (Fig. 9a), and distinctive lineaments extending across the rock slope at 300–600 m elevation (Fig. 9). An important set of NE-trending structures (S6) extends through the crest of the rock slope south of the east peak (Fig. 9); one of these structures intersects structure 1c, forming a wedge-shaped cavity (Figs. 7, 8).

4.5 Rock mass conditions

Most rocks at this site, including diorite, greenstone, and schist, are very strong (100–250 MPa) to extremely strong (> 250 MPa), requiring several blows from a geological hammer to break hand specimens. Nevertheless, weak (5–25 MPa) to strong (50–100 MPa) rocks, including argillite and marble, are also present.

Average discontinuity spacings computed from scanline data are in the range of 15–50 cm for all sets, similar to the average block sizes observed on the submarine debris cone (10–40 cm). These values represent close to moderate spacings (ISRM, 1978), which qualify the rock mass as very blocky to blocky according to Cai et al. (2004) and Marinos et al. (2005). Typical discontinuity surfaces are rough, slightly rough, or smooth; we did not observe clay-filled joints in our surveys. The typical rock mass at this site has a GSI ranging from 40 to 90, reflecting favourable rock mass conditions. Similarly, scanlines indicate RQD values in the range of 75–82 %, reflecting "FAIR" to "GOOD" rock mass conditions (Deere et al., 1967).

The observed outcrop-scale discontinuity spacing values in both dioritic and metamorphic rocks are typical of those in similar rocks described elsewhere in the Coast Mountains. Roddick (1965), for example, noted that hornblende-rich plutonic rocks, like the diorite at Adeane Point, are more closely jointed and sheeted than biotite-rich plutonic rocks. Of the hornblende-rich rocks, medium- to coarse-grained rocks have larger

NHESSD
3, 161–201, 2015

joint spacings (60–120 cm) than finer grained varieties (15–30 cm), and the smaller spacings in the finer grained intrusive rocks are similar to those in adjacent metamorphic belts.

Although average outcrop-scale joint persistence for all sets is in the range of 2–4 m, reflecting low to medium persistence (ISRM, 1978), oblique photographs of the rock slope suggest much greater persistence. Persistence "censoring" was an unavoidable reality at the outcrop scale, while in other outcrop measurements joint terminations were observed either in intact rock or against other discontinuities. Some of the more persistent structures observed in oblique photographs may represent closely spaced discontinuities separated by intact rock bridges or step-path joints.

The strong to extremely strong intact rock strength and generally favourable rock mass conditions at this site, together with the high frequency of very persistent structures, suggest that structurally controlled failure is important. Progressive stress-induced fracturing of intact rock bridges may be required to permit the larger structurally controlled failures. We would expect the dominant shape of failure surfaces to follow structures rather than involve a pseudo-circular failure surface. As a result, stability analyses based on structurally controlled failure mechanisms are considered more appropriate for this site.

5 Stability analysis

We performed a kinematic analysis based on the discontinuity system summarized in Table 1 to identify possible failure modes. Although at the individual outcrop scale, only three or four of the six sets identified might be present, all sets were considered in order to evaluate the true range of potential failure modes within different parts of the slope.

We compared the average orientation of the east and west walls to the interpreted rock mass structure to test for feasible modes of failure (Fig. 10). The most probable failure modes are planar sliding on S2 in the east wall (Fig. 10a) and wedge failure

NHESSD
3, 161–201, 2015

on the intersections of S1-S6 and S1-S3 in the west wall (Fig. 10d). However, if we account for the variability in discontinuity orientations and slope attitudes, wedge failure on the above intersections becomes feasible in the east wall and additional wedge intersections are feasible in both walls. Toppling on S6 in the east wall (Fig. 10a) and on S4 and 5 in the west wall (Fig. 10c) are also feasible if variations in discontinuity orientations are considered. Based on evidence from oblique photographs, block toppling could be an important mechanism in localized over-steepened slope sections.

Given that wedge intersections in addition to those described above daylight on relatively steep slopes, the very steep slopes in the upper part of the rock slope would appear to be the most susceptible to structurally controlled failures. Confining pressures are also lowest on this part of the slope. In this context, it is interesting to note that rockfall scars are most common near the crest of the slope.

We analyzed selected failure types identified in the kinematic analysis using SWEDGE. The orientations of S1, S2, S3, and S6, as summarized in Table 1, were used as input in the stability analysis, the results of which are expressed as stability (S_r) relative to the least stable mode (Table 2).

As is evident in Table 2, planar failure is feasible over a small range of aspects on the west slope and east wall. We call attention to the fact that the dip of S2 used in this analysis (Table 1) is based on an average for the site, and joints from this set display steeper dips near the top of the slope. Analysis with a dip angle of 55° would yield a factor of safety roughly equivalent to that observed for planar failure on S1.

Wedge failure is possible throughout the centre of the rock slope and on the periphery, covering a much wider range of aspects than planar failure. In this context, S1 is particularly important because it is involved in all three wedge combinations. S3 and S6 intersect with S1 to form steeply plunging intersections (about 50°) beneath narrow wedges, and these intersections can only occur on the steepest slopes. In contrast, the intersection between S1 and S2 forms gently plunging wedges of larger size that can form on gentler slopes. An analysis using a steeper dip on S2, as observed near the slope crest, would reduce the stability of the S1-S2 wedge, but the plunge of the

NHESSD
3, 161–201, 2015

wedge intersection (about 40°) would remain less than that formed between S1 and the steeper sets, S3 and S6.

The sketch shown in Fig. 11 illustrates two different scales of possible wedge failure at the slope crest. Considering a slope 200 m wide and 75 m high, with an orientation intermediate between that of the east and west walls (85/330°), the volumes formed from wedges defined by the intersections of S1 with S2, S3, and S6 would be 575 000, 38 000 and 38 000 m^3, respectively. This example illustrates the possible sizes of wedge failures that could occur from the upper 75 m of the rock slope. The required persistence to form these wedges would be about 300 m for the larger wedge and 100 m for the smaller wedges. The required persistence for the larger wedge is about three times that of the smaller two, therefore the large wedge failure is less likely. The lower likelihood of a larger wedge failure is due not only to the higher factor of safety but also to the lower chance of such large intersecting structures being present without the existence of significant rock bridges.

As shown in Figs. 8 and 11, a large wedge, perhaps about 0.5 Mm^3 in size, bounded below by structures 1a and 2a, is present below the west peak. It is unknown to what extent these structures persist in the subsurface, but oblique photographs suggest that structure 2a has limited persistence and does not appear to intersect structure 1a. For failure to occur in this situation, stress-induced fracturing might be required for daylighting of a through-going failure surface.

An important factor that we did not consider in our kinematic or limit equilibrium analysis is the possibility that failures could be triggered by earthquakes or intense precipitation events. These events could also contribute to progressive failure through the destruction of rock bridges along partially formed failure surfaces. Another possibility is that earthquakes or intense precipitation events might trigger numerous small failures over a wide area of the rock slope. In this way, multiple small failures could produce a larger cumulative volume of debris than would result from a single large, structurally controlled failure. Considering these factors, it is possible that the cumulative size of

NHESSD
3, 161–201, 2015

a slope failure could be significantly larger than that of one simple, structurally controlled wedge or planar failure.

6 Wave height estimate

Bornhold et al. (2007) hindcasted wave amplitudes from a past landslide at this site, assuming that the 3.5 Mm^3 submarine debris cone was emplaced by a single slide. Our study focuses on potential future landslides, and our analysis of the structure, morphology, and stability of the rock slope suggests the potential for failures of different sizes. Therefore, we have estimated wave heights from rock slope failures ranging in size from 0.5 to 3.5 Mm^3. Here, we use four of the many available forecasting methods to estimate the heights of displacement waves caused by subaerial landslides (e.g. Slingerland and Voight, 1979; Huber and Hager, 1997; Fritz et al., 2004).

Slingerland and Voight (1979) suggest that landslide velocity computed as a mass sliding on a plane (v_s) can be estimated using the following equation:

$$v_s = v_0 + \sqrt{2gs(\sin\alpha - \tan\varphi_s \cos\alpha)} \quad (1)$$

where v_0 = initial slide velocity (assumed to be zero), g = gravitational constant (9.81 $m\,s^{-2}$), s = landslide travel distance from the toe of the slide mass to the shoreline, α = slope angle in degrees, and φ_s = angle of dynamic sliding friction including pore pressure and roughness effects, with the value of $\tan\varphi_s$ assumed to be 0.25 ± 0.15. We estimated the velocities at the shoreline of slides originating from the upper part of the rock slope for different sizes of failures using Eq. (1) (Table 3). Velocities at the shoreline for failures ranging from 0.5 to 3.5 Mm^3 are 85–105 $m\,s^{-1}$.

The Froude number (F) of a landslide is a dimensionless parameter related to impact velocity (Fritz et al., 2004). In this case, F, computed from $F = v_s/(gh)^{1/2}$, ranges from 1.2 to 1.5, where g = gravitational acceleration (9.81 $m\,s^{-2}$) and h = still water depth (500 m). During acceleration to high velocities, such as is the case here, slides

NHESSD
3, 161–201, 2015

become flatter and extend in the direction of movement (Huber, 1980). The thickness of the slide mass when it entered the water was therefore estimated to be relatively small, ranging from 4 to 16 m, resulting in a slide thickness relative to water depth of 0.008 to 0.03. Using the wave classification of Fritz et al. (2003), the above values of slide Froude number, and relative slide thickness suggest that impulse waves generated would involve little to no flow separation, with no backward or forward collapsing impact craters expected from failures in this size range. We would expect wave types ranging from oscillatory (linear) to Stokes-like (nonlinear) propagating in a group, with the primary wave being the largest.

Noda (1970) developed a theoretical solution using linear wave theory to predict the form of wave motion from a rigid box falling vertically into a tank. The maximum height (η) of the primary wave is generally not developed for some distance from the impact site and can be estimated using:

$$\eta = F\lambda \tag{2}$$

where η = wave height (m), F = Froude number, and λ = maximum thickness of slide mass (m). Substituting into Eq. (2) the Froude numbers from Table 3 and the slide thicknesses from Table 4, we calculate wave heights in the range 6–20 m (Table 4).

Huber (1980) conducted an extensive study of landslide-generated impulse waves using 2-D and 3-D flume models involving granular slide masses, and formulated an empirical relation for predicting wave height outside the splash zone. In his experiments, the slide Froude number ranged from 0.5 to 3.7, the relative slide volume $[V/(bh^2)]$ was 0.03–2.57, and 1–40 % of the kinetic slide energy was converted to wave energy. Huber and Hager (1997) reanalyzed the data from Huber (1980) and generated a scaling relationship that is used here to estimate wave height (H):

$$H = 0.88 \sin\alpha \left(\frac{\rho_s}{\rho_w}\right)^{1/4} \left(\frac{v}{b}\right)^{1/2} \left(\frac{h}{x}\right)^{1/4} \tag{3}$$

NHESSD
3, 161–201, 2015

where h = still water depth (500 m), α = slide impact angle (55°), ρ_s = slide density (2600 kg m^{-3}), ρ_w = water density (1000 kg m^{-3}), V = slide volume (m^3), b = slide width upon impact with the water (m), and x = distance from impact site (m), which in this case is 2500 m to the middle of the inlet. Due to the concave plan curvature of the slope, we would expect any large failures to be channelized to some extent, producing a relatively small slide width on entry into the inlet. The slide widths summarized in Table 4 are based on an estimate of likely slide widths given the shape of the slope and the volume of the slide mass. Computed wave heights based on Eq. (3) range from 50 to 68 m (Table 4).

Fritz (2002) conducted wave-generation experiments using a pneumatic landslide generator to launch granular slides into a 2-D hydraulic model. He found that the slide Froude number is the dominant dimensionless parameter controlling wave generation, with between 2 and 30 % of the kinetic slide energy converted to the primary wave crest and 4–50 % to the wave train. He described the maximum relative wave amplitude (a_M) as:

$$\frac{a_M}{h} = \frac{1}{4} F^{\frac{7}{5}} S^{\frac{4}{5}} \tag{4}$$

where F = Froude number, h = still water depth, and S = relative slide thickness (λ/h). Substituting the slide Froude numbers in Table 3 and the slide thickness values in Table 4 into Eq. (4), we calculate maximum wave amplitudes (a_M) ranging from 5 to 11 m (Table 4). Because the expected waves will include nonlinear Stokes-like waves, the maximum wave amplitudes calculated using Eq. (4) cannot be assumed to be equal to 1/2 the wave height. A rule of thumb for non-linear slide waves found by Heller (2008) is that the wave height is 1.2 times the wave height. Using this relation, the range in maximum wave heights computed from the maximum amplitudes (a_M) in Table 4 is 6–13 m.

NHESSD
3, 161–201, 2015

Zweifel (2004) and Zweifel et al. (2006) conducted additional experiments using the same physical model as Fritz (2002). The relative maximum wave amplitude (a_M) determined from the Froude number (F), relative slide thickness (S), and the relative slide mass (M) is:

$$\frac{a_M}{h} = \frac{1}{3} F S^{\frac{1}{2}} M^{\frac{1}{4}} \quad (5)$$

where $M = m_s/(\rho_w b h^2)$, with m_s = slide mass (kg), b = width of slide mass upon entry into water (m), h = still water depth (m), and ρ_w = water density (kg m^{-3}). Maximum wave amplitudes calculated using Eq. (5) range from 11 to 22 m (Table 4), resulting in estimated maximum wave heights, using the rule of thumb of $H = 1.2a_M$, of 14 to 26 m.

In summary, we computed maximum wave heights and wave amplitudes using four different forecasting methods for rockslide volumes ranging from 0.5 to 3.5 Mm^3. The method of Huber and Hager (1997) yields much larger wave heights than the other methods. We prefer the other methods at this site because they include slide thickness as an input parameter. During acceleration to high velocities, as is expected for slides at this site, slides become flatter and stretch in the direction of movement, and the exchange of momentum from slide to water during impact occurs over a longer time (Huber, 1980). This effect is not accounted for by Huber and Hager (1997). Despite this limitation, some researchers have applied the Huber and Hager (1997) model to provide upper limits to their range of wave height estimates (Wieczorek et al., 2003, 2007). The other three models yield maximum wave heights ranging from 6 to 26 m (Table 5). Although there is uncertainty in the slide thickness used in these models, the results suggest that landslides as small as 0.5 to 1.0 Mm^3 could generate wave heights of 6 to 18 m in this high-relief setting. Waves of this size would threaten vessels and coastal infrastructure in Knight Inlet.

For the case of the 3.5 Mm^3 rockslide, Table 5 predicts wave heights of 14–26 m, whereas for the same water depth of 500 m, Bornhold et al. (2007) estimated wave heights of about 4 to 11 m. The lower estimates of wave heights in that study are

NHESSD
3, 161–201, 2015

likely related to the empirical model used, which was developed (Murty, 1979; Striem and Miloh, 1975) for submarine landslides, and to the corresponding relatively low proportion of slide kinetic energy assumed to be converted to wave energy (1–10 %) when compared with values observed from subaerial landslides. For example, through extensive experimentation using 2-D and 3-D flume models involving granular subaerial slides, Huber (1980) found that up to 40 % of the kinetic slide energy was converted to wave energy, and Fritz (2002) found that up to 30 % of the kinetic slide energy was converted to the primary wave crest.

7 Summary

The abundance of steep rock slopes towering above rockfall and rockslide deposits on the seafloor in the inner part of Knight Inlet suggests a history of tsunami-generating landslides over the past 12 000 years. A recent study integrating archaeological and geological observations with oceanographic analysis suggests that the former village of Kwalate in Knight Inlet was destroyed in the late 1500s by a landslide-induced wave. In light of this disaster, we studied the structure and stability of the rock slope across Knight Inlet from the Kwalate village to estimate likely rock-slope failure mechanisms, the size of possible future slope failures, and the heights of the resulting waves.

The contact between a Late Cretaceous dioritic pluton and a metamorphic belt consisting of greenstone of the Upper Triassic Karmutsen Formation is exposed in the rock slope at Adeane Point. The greenstone and adjacent diorite are strongly foliated, resulting in highly persistent brittle structures. Other important structures include a set of sheeting joints and highly persistent mafic dykes and faults. Stability analysis showed the potential for planar and wedge failures and highlighted the potential for wedge failures near the crest of the slope.

Kinematic and limit equilibrium analyses were performed to identify and rank the importance of different failure mechanisms and to estimate possible failure volumes. In addition to possible small failures ($< 0.5\,Mm^3$) from near the crest of the rock slope,

NHESSD
3, 161–201, 2015

much larger failures ($> 1.0\,Mm^3$) could occur, particularly with major precipitation or seismic events serving as triggers.

We estimated maximum wave heights for landslides of a range of likely sizes (0.5 to $3.5\,Mm^3$) using four different forecasting techniques. The resulting mid-inlet wave heights range from 6 to 26 m. Such waves could threaten vessels and coastal infrastructure in Knight Inlet. Given that there are several similar massive rock slopes with large submarine debris cones in the inner part of Knight Inlet, it is clear that this is an area where tsunami hazards should be considered in coastal infrastructure development and land-use planning.

Acknowledgements. Financial assistance for the project was provided by a Natural Sciences and Engineering Research Council of Canada grant to D. Stead and a graduate fellowship from Simon Fraser University to D. P. van Zeyl. The authors are grateful to Steve Israel, Dan Gibson and Bert Struik for discussions on the structural geology of the rock slope at Adeane Point.

References

Adams, J. and Atkinson, G.: Development of seismic hazard maps for the proposed 2005 edition of the National Building Code of Canada, Can. J. Civil. Eng., 30, 255–271, 2005.

Bancroft, J. A.: Geology of the coast and islands between the Strait of Georgia and Queen Charlotte Sound, British Columbia, Memoir 23, Geological Survey of Canada, Ottawa, Ontario, 1913.

Bjerrum, L. and Jørstad, F.: Stability of rock slopes in Norway, Publication 79, Norwegian Geotechnical Institute, Oslo, 1–11, 1968.

Blikra, L. H., Longva, O., Harbitz, C., and Lovhølt, F.: Quantification of rock-avalanche and tsunami hazard in Storfjorden, Western Norway, in: Landslides and Avalanches, ICFL 2005 Norway, edited by: Senneset, K., Flaate, K., and Larsen, J. O., Taylor & Francis Group, London, 57–63, 2005.

Bornhold, B. D., Harper, J. R., McLaren, D., and Thomson, R. E.: Destruction of the first nations village of Kwalate by a rock avalanche-generated tsunami, Atmos.-Ocean, 45, 123–128, 2007.

NHESSD

3, 161–201, 2015

Cai, M., Kaiser, P. K., Uno, H., Tasaka, Y., and Minami, M.: Estimation of rock mass strength and deformation modulus of jointed hard rock masses using GSI system, Int. J. Rock Mech. Min., 41, 3–19, 2004.

Canadian Hydrographic Service: Multibeam bathymetry dataset, CHSDIR File 5025887, Knight Inlet, Department of Fisheries and Oceans Canada, Canadian Hydrographic Service, Vancouver, British Columbia, 2008.

Clague, J. J.: Late quaternary geology and geochronology of British Columbia, Part 2: Summary and discussion of radiocarbon-dated quaternary history, Paper 80-35, Geological Survey of Canada, Ottawa, Ontario, 1981.

Clague, J. J.: Quaternary glaciation and sedimentation, in: Geology of the Cordilleran Orogen in Canada, edited by: Gabrielse, H. and Yorath, C. J., Geology of Canada Series 4, Geological Survey of Canada, Ottawa, Ontario, 419–434, 1991.

Dahl-Jensen, T., Larsen, L. M., Pedersen, S. A. S., Pedersen, J., Jepsen, H. F., Pedersen, G., Nielsen, J., Pedersen, A. K., Von Platen-Hallermund, F., and Weng, W.: Landslide and tsunami 21 November 2000 in Paatuut, West Greenland, Nat. Hazards, 31, 277–287, 2004.

Deere, D. U., Hendron, A. J., Patton, F. D., and Cording, E. J.: Design of surface and near surface construction in rock, in: Failure and Breakage of Rock, Proceedings, 8th US Symposium on Rock Mechanics, edited by: Fairhurst, C., Society of Mining Engineers, American Institute of Mining, Metallurgy, and Petroleum Engineers, New York, 237–302, 1967.

Dyke, A. S.: An outline of North American deglaciation with emphasis on Central and Northern Canada, in: Quaternary Glaciations, Extent and Chronology Part II: North America, edited by: Ehlers, J. and Gibbard, P. L., Elsevier, New York, 373–424, 2004.

Environment Canada: National climate archive, http://climate.weather.gc.ca/, last access: 23 September 2008.

Evans, S. G. and Clague, J. J.: Recent climatic change and catastrophic geomorphic processes in mountain environments, Geomorphology, 10, 107–128, 1994.

Fritz, H. M.: Initial phase of landslide generated impulse waves, PhD thesis, Swiss Federal Institute of Technology, Zürich, 2002.

Fritz, H. M., Hager, W. H., and Minor, H.-E.: Landslide generated impulse waves, Exp. Fluids, 35, 505–532, 2003.

Fritz, H. M., Hager, W. H., and Minor, H.-E.: Near field characteristics of landslide generated impulse waves, J. Waterw. Port C.-ASCE, 130, 287–302, 2004.

NHESSD

3, 161–201, 2015

GeoBase: Canadian digital elevation data (CDED), http://www.geobase.ca, last access: 8 February 2008.
Gilbert, R.: Engineering consultant raises concerns over Porteau Bluff, Journal of Commerce, 18 August 2008.
Heller, V.: Landslide generated impulse waves: Prediction of near field characteristics, PhD thesis, Swiss Federal Institute of Technology, Zürich, 2008.
Hoek, E. and Bray, J. W.: Rock Slope Engineering, 3rd Edn., Institute of Mining and Metallurgy, London, 1981.
Hoek, E., Carranza-Torres, C., and Corkum, B.: Hoek-Brown criterion – 2002 edition, in: Proceedings, NARMS-TAC Conference, Toronto, Ontario, 1, 267–273, 2002.
Huber, A.: Schwallwellen in Seen als Folge von Felsstürzen, PhD thesis, Swiss Federal Institute of Technology, Zürich, 1980.
Huber, A.: Felsbewegungen und Uferabbrüche an Schweizer Seen, ihre Ursachen und Auswirkungen, Eclogae Geol. Helv., 75, 563–578, 1982.
Huber, A. and Hager, W. H.: Forecasting impulse waves in reservoirs, in: Proceedings, 19th Congrès des Grands Barrages, C.31, ICOLD, Paris, 993–1005, 1997.
ISRM: Suggested methods for the quantitative description of discontinuities in rock masses, Int. J. Rock Mech. Min., 15, 319–368, 1978.
Marinos, V., Marinos, P., and Hoek, E.: The geological strength index: applications and limitations, B. Eng. Geol. Environ., 64, 55–65, 2005.
Mathews, W. H.: Ice sheets and ice streams: thoughts on the Cordilleran Ice Sheet Symposium, Geogr. Phys. Quatern., 45, 263–267, 1991.
Miller, D. J.: The Alaska earthquake of 10 July 1958: giant wave in Lituya Bay, B. Seismol. Soc. Am., 50, 253–266, 1960a.
Miller, D. J.: Giant waves in Lituya Bay, Alaska, Professional Paper 354-C, US Geological Survey, Denver, Colorado, 51–87, 1960b.
Murty, T. S.: Submarine slide-generated water waves in Kitimat, British Columbia, J. Geophys. Res., 84, 7777–7779, 1979.
Noda, E.: Water waves generated by landslides, J. Waterways Harbors Coast Eng. Div., 96, 835–855, 1970.
Rocscience: SWEDGE, Rocscience Inc., Toronto, Ontario, 2008.

NHESSD
3, 161–201, 2015

Roddick, J. A.: Vancouver North, Coquitlam, and Pitt Lake map-areas, British Columbia, with special emphasis on the evolution of the plutonic rocks, Memoir 335, Geological Survey of Canada, Ottawa, Ontario, 1965.
Roddick, J. A.: Notes on the stratified rocks of Bute Inlet map-area (excluding Vancouver and Quadra islands), Open File 480, Geological Survey of Canada, Ottawa, Ontario, 1977.
Roddick, J. A. and Hutchison, W. W.: Setting of the coast plutonic complex, British Columbia, Pacific Geology, 8, 91–108, 1974.
Roddick, J. A. and Woodsworth, G. J.: Geology, Bute Inlet, British Columbia, Open File 5037, Geological Survey of Canada, Ottawa, Ontario, 2006.
Sepúlveda, S. A., Serey, A., Lara, M., Pavez, A., and Rebolledo, S.: Landslides induced by the April 2007 Aysén fjord earthquake, Chilean Patagonia Landslides, 7, 483–492, 2010.
Slingerland, R. L. and Voight, B.: Occurrences, properties, and predictive models of landslide-generated water waves, in: Rockslides and Avalanches, vol. 2, edited by: Voight, B., Elsevier, New York, 317–397, 1979.
Striem, H. L. and Miloh, T.: Tsunamis induced by submarine slumpings off the coast of Israel, Report IA-LD-1-102, Israel Atomic Energy Commission, Tel Aviv, 1975.
Terzaghi, K.: Stability of steep slopes on hard unweathered rock, Géotechnique, 12, 251–270, 1962.
van Zeyl. D. P.: Evaluation of subaerial landslide hazards in Knight Inlet and Howe Sound, British Columbia, MSc thesis, Simon Fraser University, Burnaby, British Columbia, 2009.
Wieczorek, G. F., Jakob, M., Motyka, R. J., Zirnheld, S. L., and Craw, P.: Preliminary assessment of landslide-induced wave hazards: Tidal Inlet, Glacier Bay National Park, Alaska, Open File Report 03-100, US Geological Survey, Denver, Colorado, 2003.
Wieczorek, G. F., Geist, E. L., Motyka, R. J., and Jakob, M.: Hazard assessment of the Tidal Inlet landslide and potential subsequent tsunami, Glacier Bay National Park, Alaska, Landslides, 4, 205–215, 2007.
Woodsworth, G. J., Monger, J. W. H., and Gabrielse, H.: Part B, Coast Belt, Chapter 17, Structural styles, in: Geology of the Cordilleran Orogen in Canada, edited by: Gabrielse, H. and Yorath, C. J., Geology of Canada Series 4, Geological Survey of Canada, Ottawa, Ontario, 581–591, 1991.
Wyllie, D. C. and Mah, C. W.: Rock Slope Engineering: Civil and Mining, 4th Edn., Taylor & Francis, New York, 2003.

NHESSD
3, 161–201, 2015

Zweifel, A.: Impulswellen: Effekte der Rutschdichte und der Wassertiefe. PhD thesis, Swiss Federal Institute of Technology, Zürich, 2004.
Zweifel, A., Hager, W. H., and Minor, H.-E.: Plane impulse waves in reservoirs, J. Waterw. Port C.-ASCE, 132, 358–368, 2006.

NHESSD
3, 161–201, 2015

Table 1. Summary of interpreted discontinuity sets.

Set	D/DD (°)	Type
S1	54/028	Foliation, bedding, faults
S2	36/281	Unloading joints
S3	86/083	Joints, veins
S4	43/159	Joints, veins
S5	76/338	Joints, dykes
S6	80/295	Joints, dykes, faults

NHESSD
3, 161–201, 2015

Table 2. Results of stability analysis.

Failure type	S_r	Aspect (°)[1]	Slope (°)[2]	Walls[3]
Planar S1	1.0	30	55	WS
Wedge S1-S6	1.2	90	55	WS, WW, EW
Wedge S1-S3	1.9	105	55	WS, WW, EW
Planar S2	1.9	15	45	EW
Wedge S1-S2	3.0	105	30	WS, WW, EW

[1]Range in aspect where failure type is feasible.
[2]Minimum slope in which failure type is feasible.
[3]Walls in which failure type is feasible:
WS = west slope WW = west wall EW = east wall.

NHESSD
3, 161–201, 2015

Table 3. Estimated slide velocity at shoreline.

V (Mm^3)	s (m)	v_s ($m\,s^{-1}$)	F
0.5	825	105	1.5
1.0	800	103	1.5
1.5	750	100	1.4
2.0	700	96	1.4
2.5	675	95	1.4
3.0	600	89	1.3
3.5	550	85	1.2

NHESSD
3, 161–201, 2015

Table 4. Estimated maximum wave heights and amplitudes.

V (Mm^3)	λ (m)	η (m)	b (m)	H (m)	a_m (m)[1]	a_m (m)[2]
0.5	4	6	75	50	5	11
1.0	6	9	125	55	6	14
1.5	8	11	175	57	7	16
2.0	10	14	225	58	9	18
2.5	12	16	275	58	10	19
3.0	14	18	325	59	10	20
3.5	16	20	280	68	11	22

V = slide volume
λ = maximum slide thickness (Eq. 2)
η = maximum wave height (Eq. 2)
b = slide width upon impact with water (Eq. 3)
H = maximum wave height (Eq. 3)
[1] a_m = maximum relative wave amplitude (Eq. 4)
[2] a_m = maximum relative wave amplitude (Eq. 5)

NHESSD
3, 161–201, 2015

Table 5. Estimated maximum wave heights (m).

V (Mm^3)	Noda (1970)	Fritz (2002)	Zweifel (2004)
0.5	6	6	13
1.0	9	7	17
1.5	11	8	19
2.0	14	11	22
2.5	16	12	23
3.0	18	12	24
3.5	20	13	26

V = slide volume

NHESSD
3, 161–201, 2015

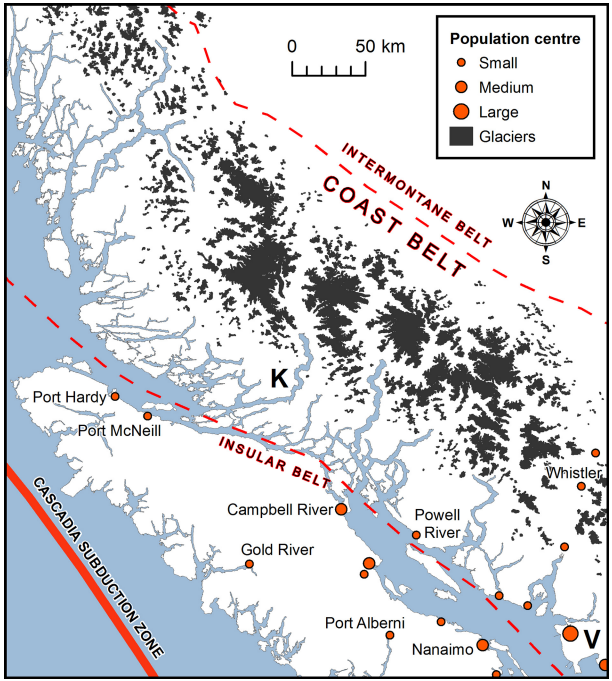

Figure 1. Location of Knight Inlet (K) on the southern British Columbia coast. Glaciers coincide with the highest parts of the Coast Mountains. V = Vancouver.

NHESSD
3, 161–201, 2015

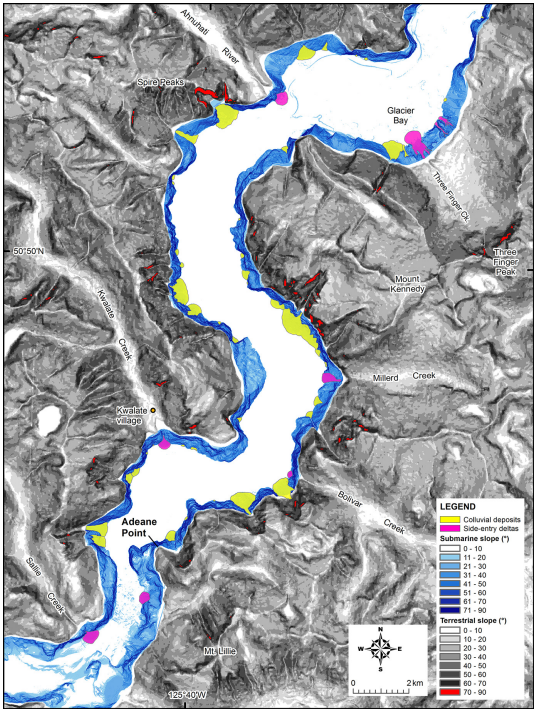

Figure 2. Terrestrial and submarine topography of the middle part of Knight Inlet, showing many colluvial deposits beneath steep rock slopes and side-entry deltas at the mouths of tributary streams. Many of the seafloor deposits mapped in this figure are hybrid colluvial/alluvial landforms; the alluvial deposit beneath Three Finger Creek, for example, contains material from a rock slope failure at Three Finger Peak that caused a wave in November 1999 that was felt 20 km to the north at the head of Knight Inlet. SONAR data used to generate DEM were provided by the Canadian Hydrographic Service (2008).

NHESSD
3, 161–201, 2015

Figure 3. Oblique photograph of the rock slope at Adeane Point. WS = west slope; c = central gully; w = west gully.

NHESSD
3, 161–201, 2015

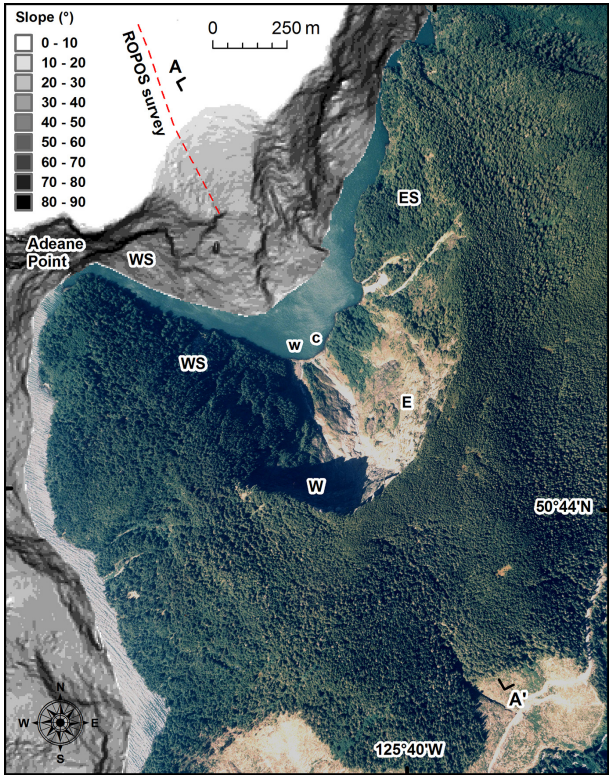

Figure 4. Vertical image showing the subaerial and submarine parts of the rock slope at Adeane Point. The offshore area is represented by a slope map generated from swath bathymetry. WS = west slope, W = west wall, w = west gully, c = central gully, E = east wall, ES = east slope, n = north gully.

NHESSD
3, 161–201, 2015

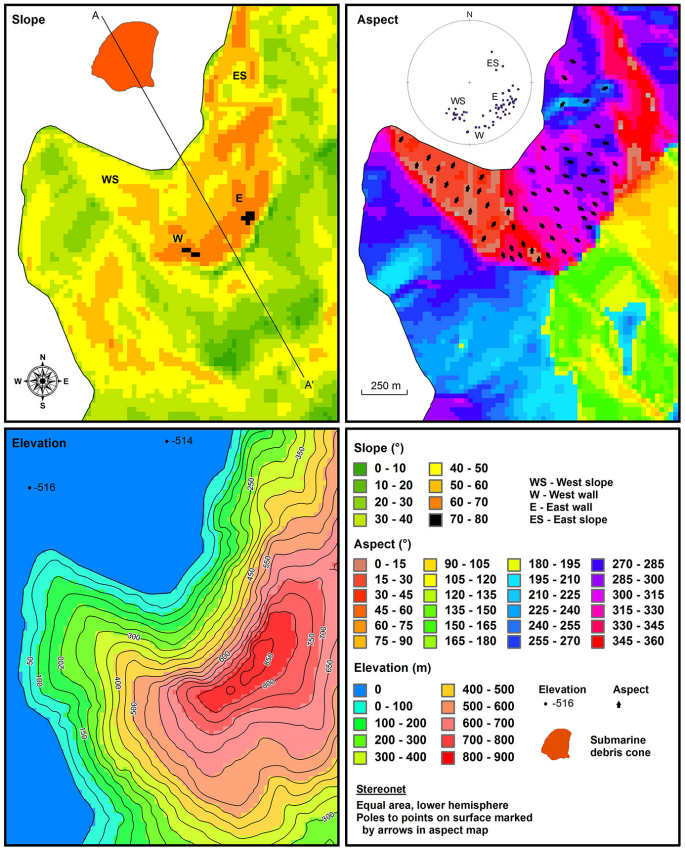

Figure 5. Slope and aspect maps. Stereonet included with the aspect map shows the three-dimensional shape of the slope.

NHESSD
3, 161–201, 2015

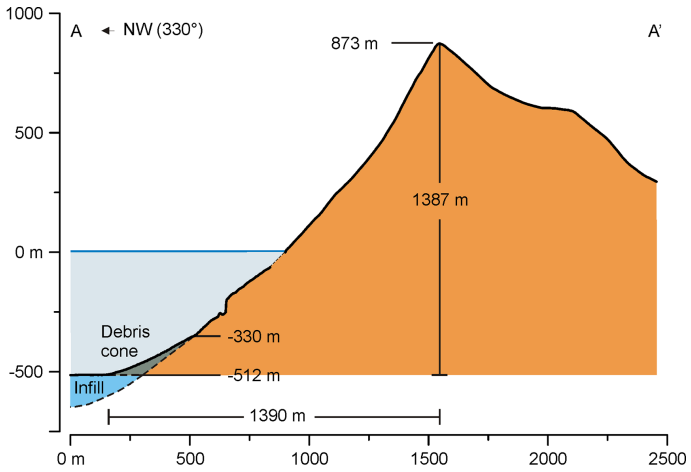

Figure 6. Profile of the rock slope at Adeane Point, including a schematic representation of submarine debris cone and fjord infill sediments.

NHESSD
3, 161–201, 2015

Structure, stability and tsunami hazard associated with a rock slope in Knight Inlet

D. P. van Zeyl et al.

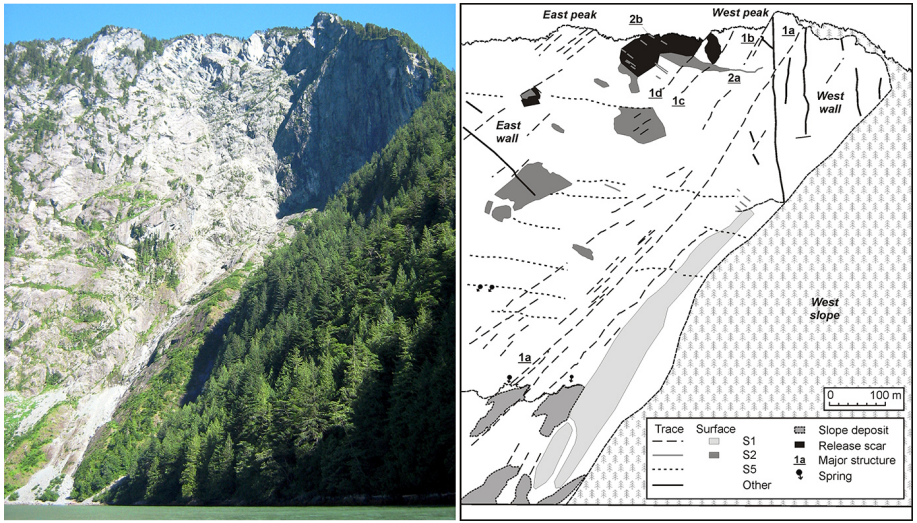

Figure 7. Left panel: Oblique view of rock slope. Right panel: map showing major structures exposed in the slope.

NHESSD
3, 161–201, 2015

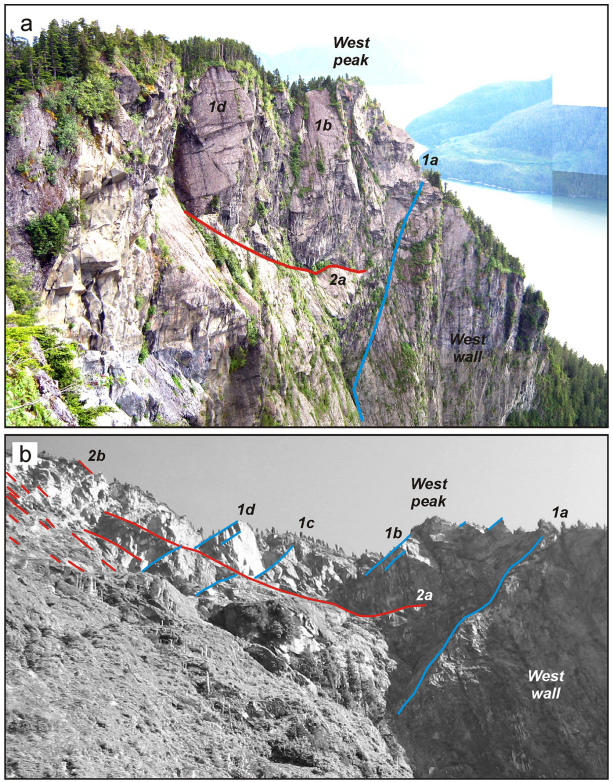

Figure 8. Oblique photographs showing major structures at the crest of the rock slope. See text for explanation of discontinuity sets.

NHESSD
3, 161–201, 2015

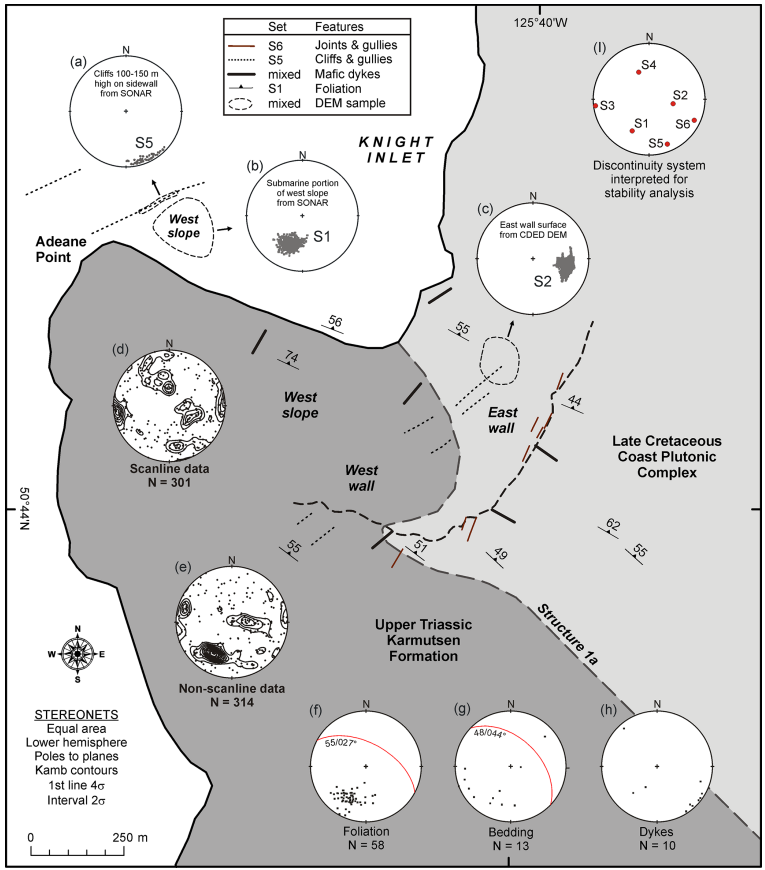

Figure 9. Synthesis of field and remotely sensed structural data.

NHESSD
3, 161–201, 2015

Structure, stability and tsunami hazard associated with a rock slope in Knight Inlet

D. P. van Zeyl et al.

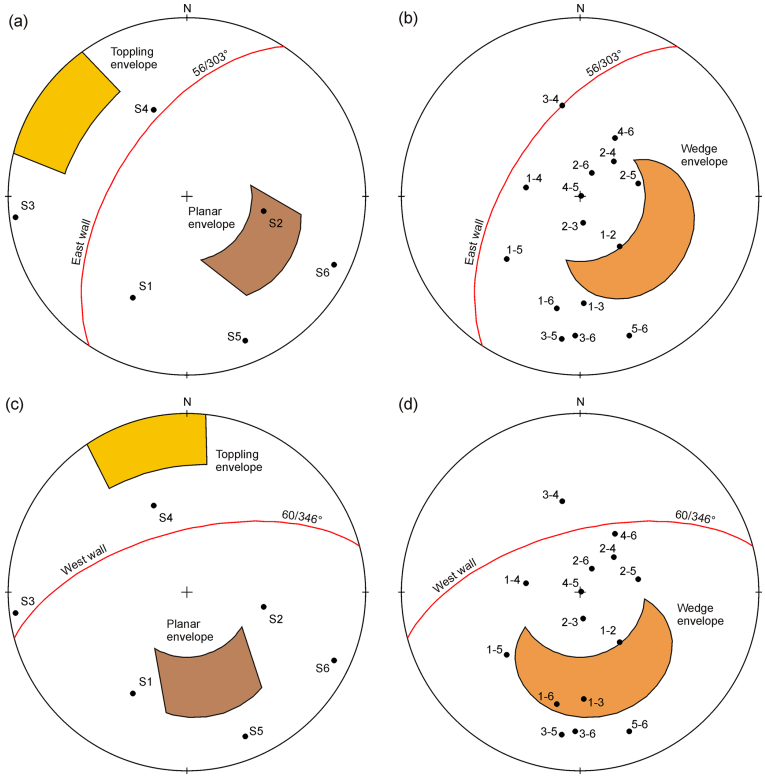

Figure 10. Equal-area lower hemisphere stereonets showing **(a)** the planar and toppling check for the east wall, **(b)** the wedge failure check for the east wall, **(c)** the planar and toppling check for the west wall, and **(d)** the wedge failure check for the west wall **(d)**. A 30° friction cone is assumed.

NHESSD
3, 161–201, 2015

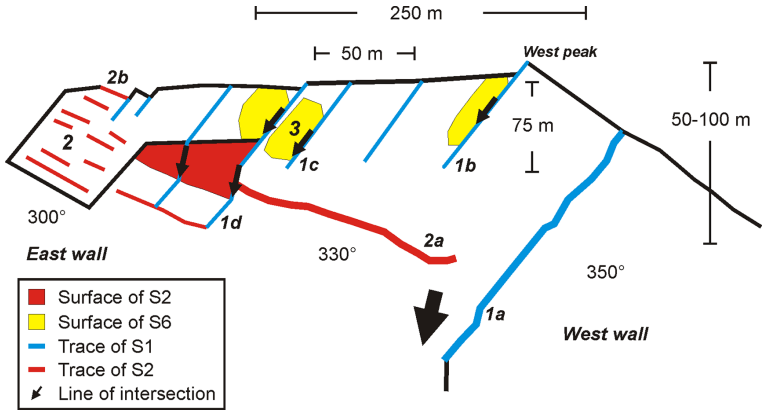

Figure 11. Cartoon showing two scales of wedge-shaped blocks at the crest of the rock slope at Adeane Point. Wedges formed by S1-S6 have dimensions of 50–75 m. The large wedge formed by S1-S2 has dimensions of about 75 and 250 m. Azimuths are the dip directions of the rock slope at the respective locations.

NHESSD
3, 161–201, 2015